The Astrophysical Journal, 977:171 (14pp), 2024 December 20 https://doi.org/10.3847/1538-4357/ad8dd3

Low-latitude Auroras: Insights from 2023 April 23 Solar Storm

Geeta Vichare[1], Ankush Bhaskar[2], Rahul Rawat[1], Virendra Yadav[3], Wageesh Mishra[4], Dorje Angchuk[4], and Anand Kumar Singh[5]
[1] Indian Institute of Geomagnetism, Navi Mumbai, Maharashtra, India; geeta.vichare@iigm.res.in
[2] Space Physics Laboratory, ISRO/Vikram Sarabhai Space Centre, Thiruvananthapuram, India
[3] Aryabhatta Research Institute of Observational Sciences, Nainital, Uttarakhand, India
[4] Indian Institute of Astrophysics, Bengaluru, Karnataka, India
[5] National Centre for Polar and Oceanic Research, Goa, India
Received 2024 April 16; revised 2024 October 21; accepted 2024 October 21; published 2024 December 11

Abstract

In 2023 April, a low-latitude aurora observed by the all-sky camera at Hanle, Ladakh, India (33°14'N geographic latitude), generated significant interest. This was the first such aurora recorded from the Indian region in the space era and occurred during a moderate solar storm. This study explores this low-latitude auroral sighting, which happened during the sheath-region passage of an interplanetary coronal mass ejection. We analyze in situ multispacecraft particle measurements and geomagnetic field observations from both ground-based and satellite-based magnetometers. The auroral observations at Hanle coincided with intense substorm activity. Our findings indicate that the aurora did not actually reach India; the equatorward boundary was beyond 50°N geographic latitude. Enhanced electron fluxes with energies below 100 eV were detected at 54°N geographic latitude at about 830 km altitude in the predawn sector (4–5 hr local time). In the midnight sector, the equatorward boundary is estimated to be around 52°N geographic latitude, based on Hanle observations and considering emission altitudes of 600–650 km due to low-energy electrons. Thus, the low-latitude red aurora observed from India resulted from the emissions at higher altitudes due to low-energy electron precipitation in the auroral oval and a slight equatorward expansion of the auroral oval. The low-energy electrons likely originated from the plasma sheet and were precipitated due to enhanced wave–particle interactions from strong magnetosphere compression during high solar wind pressure. This study is crucial in understanding low-latitude auroras in the modern space era.

Unified Astronomy Thesaurus concepts: Aurorae (2192); Solar particle emission (1517); Solar storm (1526); Solar coronal mass ejections (310)

1. Introduction

The plasma particles and electromagnetic fields of solar origin interact with the Earth's magnetic field, leading to several space weather phenomena such as geomagnetic storms, substorms, and visible auroras (W. D. Gonzalez et al. 1994; J. U. Kozyra & M. W. Liemohn 2003; A. Bhaskar & G. Vichare 2013; E. K. J. Kilpua et al. 2015; A. N. Raghav et al. 2018; L. Dai et al. 2023). There have been several solar storms producing geomagnetic storms on the Earth and even low-latitude auroras (S. M. Silverman 2003; R. Hajra & B. T. Tsurutani 2018; H. Hayakawa et al. 2018a, 2022, 2023; G. Wang et al. 2021). The solar energy injected into the Earth's magnetosphere through coupling gets distributed in various regions of the magnetosphere (G. Vichare et al. 2005). The substorms are electrodynamic events that occur in the Earth's magnetosphere–ionosphere system, characterized by intense auroral displays in the latitudinal ring between ∼60° and 75° in both hemispheres, also known as the "auroral oval" (S.-I. Akasofu 1964; G. Rostoker et al. 1980; D. N. Baker et al. 1996). The aurora borealis (northern lights) is visible around the Arctic Ocean, and the aurora australis (southern lights) is mainly observed in Antarctica and sometimes in Australia. When fluxes of energetic electrons and protons precipitate along the magnetic field lines to enter into the Earth's atmosphere, auroral emissions occur. An increase in the convective electric field produces intense currents in the ionosphere, giving rise to auroral electrojets, monitored through magnetic field measurements (R. L. McPherron 1972; P. Newell & J. Gjerloev 2011; J. K. Behera et al. 2015). Isolated proton aurora (IPA), strong thermal emission velocity enhancement (STEVE), and stable auroral red (SAR) are the most prominent optical emissions in the subauroral regions (B. Gallardo-Lacourt et al. 2021; Y. Nishimura et al. 2022). IPA is found to be caused by fine-structured EMIC Pc1 waves (K. Sakaguchi et al. 2015; R. Nomura et al. 2016; H. Kim et al. 2021). SAR arcs are considered to be due to energy transfer from the ring current to the hot plasma in the outer plasmasphere (K. D. Cole 1965; J. U. Kozyra et al. 1997). STEVE is a heated glowing gas created by very fast plasma streams and appears as streaks in the sky during auroral activity (E. A. MacDonald et al. 2018). Moreover, K. Shiokawa et al. (1997) showed that the precipitation of broadband electrons (BBEs) is responsible for the red aurora at midlatitudes.

P.-H. Lee & J.-Y. Liu (2023) examined the long historical records from China and found that the red auroras were quite frequent during high solar activity periods. However, there are reports of mid-to-low-latitude auroras during relatively calm or moderately active geomagnetic conditions (e.g., J. M. Vaquero et al. 2007, 2013; D. Willis et al. 2007; H. Hayakawa et al. 2018b; A. Bhaskar et al. 2020; D. M. Oliveira et al. 2020; G. Wang et al. 2021). S. M. Silverman (2003) categorized these auroras as "sporadic auroras." These auroras are typically faint, and their specific characteristics, including duration and their

association with compression of the magnetosphere and substorms, are subjects of ongoing investigation (S. M. Silverman 2003; H. Hayakawa et al. 2018b; A. Bhaskar et al. 2020; D. M. Oliveira et al. 2020). While the precise mechanisms behind these auroras remain incompletely understood, it is of paramount importance to observe such events during the modern era when several state-of-the-art space- and ground-based observing facilities are available. Before the auroral report in 2023 April, no auroral observations from India had been documented during the space era. Auroral observations in India are exceedingly rare, as it is situated in low latitudes. However, during the extreme geomagnetic storm event of 1872, an aurora was observed in Mumbai and other low-latitude cities (M. P. Rao 1964; S. M. Silverman 2008; C. Uberoi 2011; H. Hayakawa et al. 2018a). While most of the sporadic or low-latitude auroral observations are reported before the space age and inferred from historical records, the present study provides an opportunity to investigate the low-latitude auroral observations for one of the recent moderate-level geomagnetic storms.

On the night of 2023 April 23–24, a 360° all-sky camera located at Hanle in Ladakh, India, observed a red aurora. This observation of an aurora at such a low latitude during a moderate geomagnetic storm was intriguing. Since auroras and airglow both are naturally occurring luminescent phenomena in the Earth's atmosphere, the first task was to confirm that the observed red emission to the north of Hanle was not airglow. There is a basic difference between these two; i.e., the aurora appears due to the interaction between energetic particles and the ionosphere, while airglow is caused by solar radiation. Airglow is relatively fainter and occurs globally and at all times, whereas an aurora appears during substorms. Hanle observation sources reported that the observed red emission was not airglow (ET Online and Agencies 2023). In this communication, we investigate this event in detail using satellite-based measurements of particle flux and field-aligned currents (FACs) and ground-based magnetic field observations to unravel the mystery of auroral observations at low latitudes.

2. Hanle Observations

The Indian Institute of Astrophysics (IIA) shared the video of the aurora taken from the all-sky camera at Hanle for the 2023 April event on X (earlier Twitter; IIABengaluru 2023). Hanle is a village in Ladakh, India, situated at an altitude of 14,764 feet above sea level and devoid of artificial city light. The position coordinates of Hanle are as follows: geographic latitude (GGLat) = 32.8°N, geographic longitude (GGLon) = 79°E, geomagnetic latitude (GMLat) = 24.4°N, and geomagnetic longitude (GMLon) = 154°E. Following IIA's report on the aurora at Ladakh, false pictures claiming to be the recent aurora in Ladakh were spread on social media (ABPLive 2023). However, those were old pictures taken in Norway and Iceland, not in Ladakh (A. Anand 2023). In fact, the Ladakh aurora of 2023 April was subvisual, observed by the all-sky camera. It is necessary to take appropriate precautions while posting on social media. Upon the 2024 May supergeomagnetic storm, similar false reporting might have happened, and it is necessary to avoid such things.

Figure 1 shows the actual picture of the aurora (red glow at the top side of the image) seen by the all-sky camera at Hanle at 1:24 IST on April 24 (19:54 UT on April 23). The red light that appeared to the north of Hanle has a zenith angle of ∼80°−85° N. This indicates that the aurora has not occurred over Hanle but at higher latitudes. The red emission was observed from 19:30 (01:00 IST) until 22:00 UT (03:30 IST), and later on it became very faint. At 22:30 UT (04:00 IST), it appeared pinkish. It may be noted that the observations of the night sky or aurora from the all-sky camera at Hanle are possible during the dark hours only, and observations during sunlit hours are masked by the sunlight. The elevation angle of the red emission at Hanle seen in Figure 1 is computed using background star positions and a simulated view of the night sky at Hanle using Stellarium planetarium software. The elevation angle of the top edge of the red glow was found to be around 6°–8°.

3. Interplanetary and Geomagnetic Conditions

On 2023 April 21, an M1.7 class solar flare followed by a coronal mass ejection (CME) was ejected from the Sun, causing a moderate geomagnetic storm on April 23–24 on the Earth (P. Vemareddy 2024). Figure 2 shows the interplanetary parameters and Sym-H index during 2023 April 23–24. After 8 UT on 23 April, the north–south component (Bz) of the interplanetary magnetic field (IMF) turned southward and remained southward for several hours, facilitating the magnetic field reconnection at the Earth's magnetopause. However, a sharp southward turning of IMF Bz occurred just before 18 UT, resulting in an enhanced geomagnetic disturbance on Earth. The sheath region of the interplanetary CME (ICME; shaded pink) showed elevated plasma parameters and some quasi-planarity structure (K. Ghag et al. 2024). The geomagnetic storm monitored by the Sym-H index indicates that the ring current started developing slowly from 9 UT on April 23, as the IMF Bz component was almost −10 nT, and then before 18 UT, the ring current strengthened due to further southward turning of the IMF, with the corresponding eastward component of the interplanetary electric field (E_{sw}) reaching ∼15 mV m^{-1}. This is also accompanied by a sudden increase in the solar wind dynamic pressure (P_{sw}), resulting in sudden commencement at 17:35 UT. At 21 UT, the IMF turned northward. The geomagnetic storm index Sym-H attained a value of −175 nT at ∼22 UT. Later, on April 24, the IMF Bz turned southward (>30 nT), giving a stronger E_{sw} exceeding 20 mV m^{-1}; consequently, Sym-H became stronger crossing −200 nT. The plasma beta and temperature parameters during this time indicate the passage of the magnetic cloud of the ICME. Thus, the disturbance in Sym-H of ∼−175 nT on April 23 is mainly caused during the passage of the sheath region of the ICME, whereas further enhancement of the ring current with Sym-H = −200 nT on April 24 is caused by the magnetic cloud of the ICME (shaded in violet color).

Figure 3 depicts the AL, AU, AE, and AO indices (preliminary) obtained from WDC Kyoto and the SML and SMU indices from SuperMAG.[6] The geomagnetic disturbances in the H component, as observed at 10–12 longitudinally distributed observatories located in the auroral zone of the Northern Hemisphere, are used to derive the auroral electrojet indices (T. N. Davis & M. Sugiura 1966). The sudden decrease in the AL index indicates the start of the substorm expansion phase and defines the substorm onset time. From Figure 3, it can be observed that on April 23, the substorm activity was enhanced after 10 UT. It can be noticed that there were

[6] https://supermag.jhuapl.edu/

Figure 1. Aurora seen on 2023 April 23 by the all-sky camera from Hanle, Ladakh, India (GGLat: 32.8°N, GGLon: 79°E; GMLat: 24.4°N, GMLon: 154°E), at 19:54 UT. The north direction is upward. The red diffuse glow is visible on the top side at Hanle.

episodes of supersubstorms with AL/SML reaching −1500 nT during 18–22 UT (23:30–3:30 IST). Thus, during the night of April 23 over Indian longitudes, there was the occurrence of substorms.

4. Magnetic Field Variations

In addition to high latitudes, midlatitude magnetic field measurements are also used to study the substorm-associated current system. The substorm current wedge (SCW) produces systematic positive H variations at midlatitudes (also called the positive bay) on the nightside, particularly between 21 and 02 local time (LT) hours, at the time of the substorm expansion phase (R. L. McPherron et al. 1973; C. R. Clauer & R. L. McPherron 1974; A. D. DeJong et al. 2007). Figure 4 shows the variation of the H component at the observatories from the eastern Asian region (70°−115°E longitude) during 17–22 UT on 2023 April 23. This time window represents the local night in this sector. Table 1 shows the list of observatories used along with the geographic (GG) and geomagnetic coordinates. Here GMLats are dipole magnetic latitudes. Figure 4 displays the geomagnetic variations from mid-to-low-latitude stations (alternate red and blue curves) in two panels. For comparison purposes, the Sym-H index is plotted topmost on the left panel (magenta color). As discussed in Section 3, the ICME shock at ∼17:35 UT has resulted in a sudden increase in the H component on the ground, which is also reflected in the Sym-H index. This was followed by the ring current development, which is seen as a declining H component in almost all the plots. Though several episodes of substorm activity occurred during this time, the midlatitude variations are complex due to an ongoing geomagnetic storm; hence, it is difficult to identify a substorm-associated positive bay. The figure presented in the supplementary material (Figure A1), obtained by applying a bandpass filter between 5 and 25 mHz, shows the presence of Pi2 pulsations during 19–21 UT, confirming the substorm activity. The H component between the vertical dashed lines in Figure 4 depicts positive variations at the stations shown in the left panel and negative variations at the stations shown in the right panel. This time interval is accompanied by the solar wind pressure increase ($\delta P_{sw} = 9$ nPa at 19.2 UT), compressing the magnetospheric cavity ($\delta MP = -0.5\ R_E$); accordingly, the Sym-H index registered an increase of ∼25 nT. However, the stations in the left panel show a positive signature with an amplitude of ∼50 nT. The magnetic measurements at Indian stations from GUL to TIR and further crossing into the Southern Hemisphere up to 21°S GMLat show a positive variation of ∼50 nT amplitude. This higher amplitude could be due to the additional effect of the positive bay associated with the substorm. The presence of Pi2 activity at ∼19.5 UT suggests the expansion phase of the

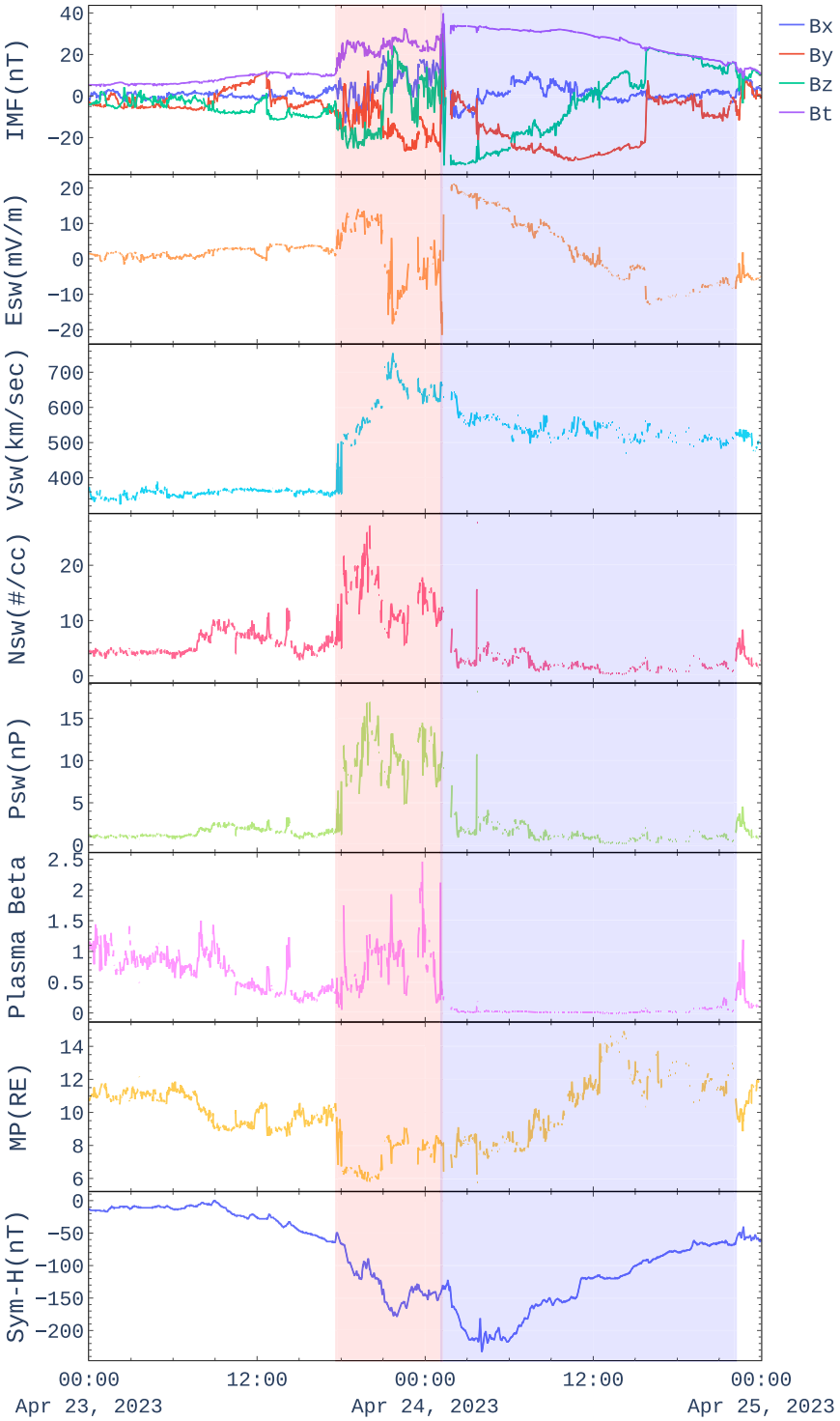

Figure 2. Interplanetary and solar wind parameters along with magnetopause distance (MP) and geomagnetic activity index Sym-H during 2023 April 23–24. The shaded regions in pink and violet indicate the sheath and magnetic cloud regions of the ICME, respectively.

substorm. The plots in the right panel show a decrease between two vertical dashed lines. The NVS, IRT, and BMT stations located north of the Indian stations show a strong negative excursion. The negative variation is strongest at NVS (GMLat = 46°N) of ∼250 nT and is observed at lower latitudes up to BMT, located at 31°N GMLat, with an amplitude of ∼50 nT. Similarly, in the Southern Hemisphere, the LRM and GNG stations with GMLat of 31.3°S and 40.34°S showed negative excursions of magnitudes 75 nT and ∼100 nT, respectively. All five stations shown in the right panel are midlatitude stations with GMLat $< 50°$ located near midnight, where positive H variation is expected. Apart from this, positive signatures at those stations are anticipated due to the solar wind pressure impulse, but we observe a negative dip reaching up to 31°N and 31.3°S GMLat. We further investigate this event using particle flux data and FACs, particularly in the time window between 19 and 20 UT, for identifying the equatorward boundary of an auroral electrojet.

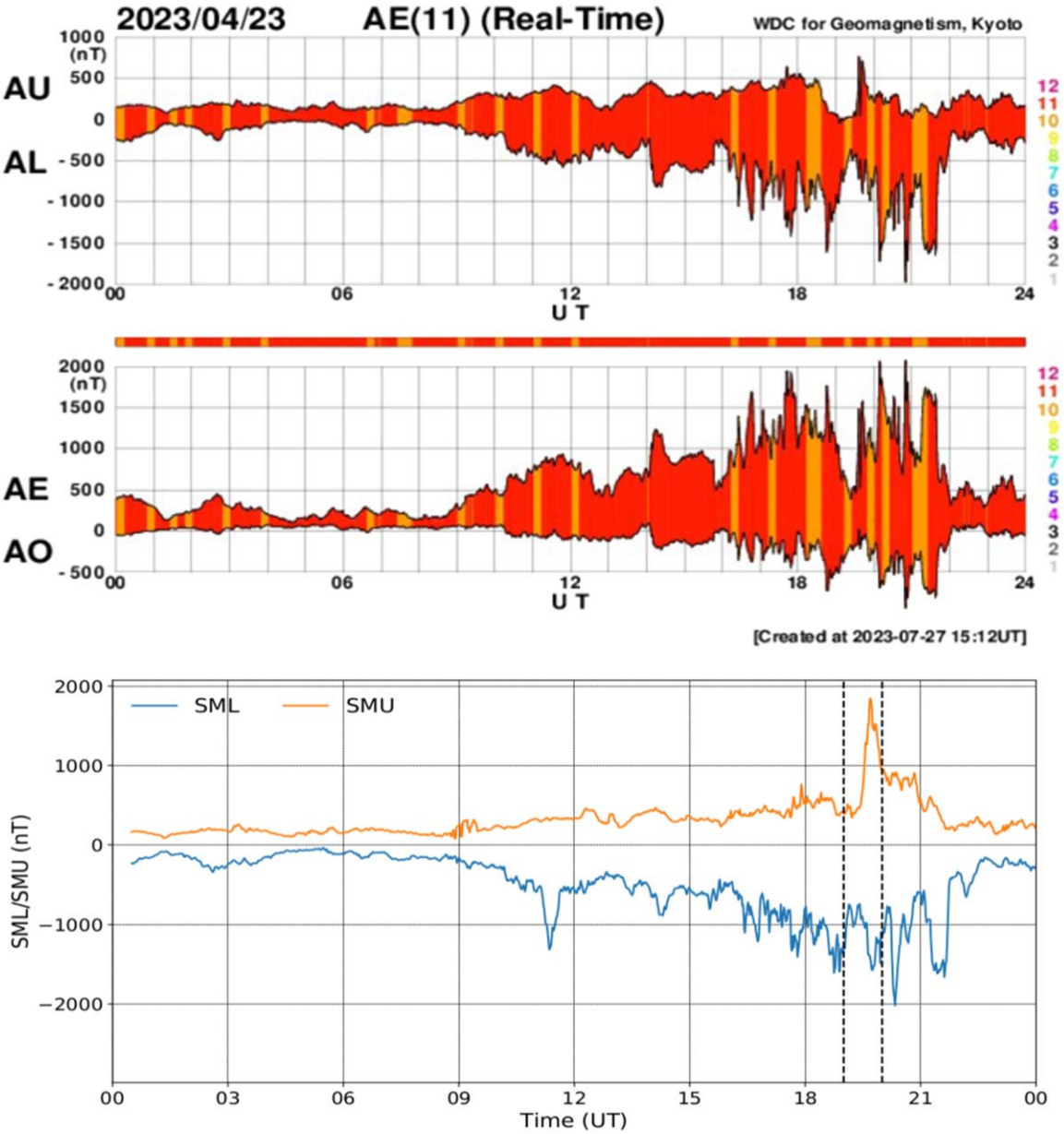

Figure 3. (Top two panels) Preliminary auroral electrojet indices on 2023 April 23 obtained from WDC, Kyoto. (Bottom panel) SMU and SML indices representing auroral activity obtained from SuperMAG. The peak of the eastward electrojet (SMU index) coincides with the Hanle observations of the aurora.

5. Estimation of the Equatorward Boundary of the Auroral Oval

5.1. Observations of Particle Flux by NOAA Polar-orbiting Operational Environmental Satellites

NOAA Polar-orbiting Operational Environmental Satellites (POES) are low-Earth-orbiting satellites at ∼850 km altitude with nearly circular, Sun-synchronous polar orbits with an orbital period of ∼102 minutes. The Medium Energy Proton and Electron Detector instrument on board the POES satellites measures energetic protons and electrons >30 keV in two orthogonal directions. Figure 5 shows the trajectories of NOAA satellites (N15, N18, and N19) and Metop1 satellites in the GMLat–time frame from 19 to 20 UT on 2023 April 23. Figure 6 displays the particle flux in the GMLat–GGLon frame of 0° directed (precipitating) electron (left) and proton fluxes (right) of different energies observed by N15, N18, N19, and Metop1 during 19–20 UT on April 23. Note that the *X*-axis shows GGLon, while the *Y*-axis represents GMLat. In the Northern Hemisphere, all these satellites cross the auroral oval equatorward boundary at ∼20° and ∼180° GGLon. The satellites passing near 20° GGLon have an LT of around 20–21 hr, while those passing over 180° GGLon have ∼7–8 LT. The maximum precipitating flux is $\sim 10^5$ (shown in red) and is located beyond 50° GMLat latitude. That means the equatorward auroral boundaries have not reached lower than 50° GMLat. In the Northern Hemisphere, the electrons with 40 keV energy indicate the equatorward boundary of precipitation as 54°N GMLat, and the proton flux of energy of 39 keV shows this boundary at ∼53°N GMLat. It is noticed that lower-energy protons (40 keV) have considerable flux (a few thousand) at low latitudes in N18 and M1 satellites, which traversed near midnight, while electrons showed minimum flux therein. The proton flux in the N15 and N19 satellite passes

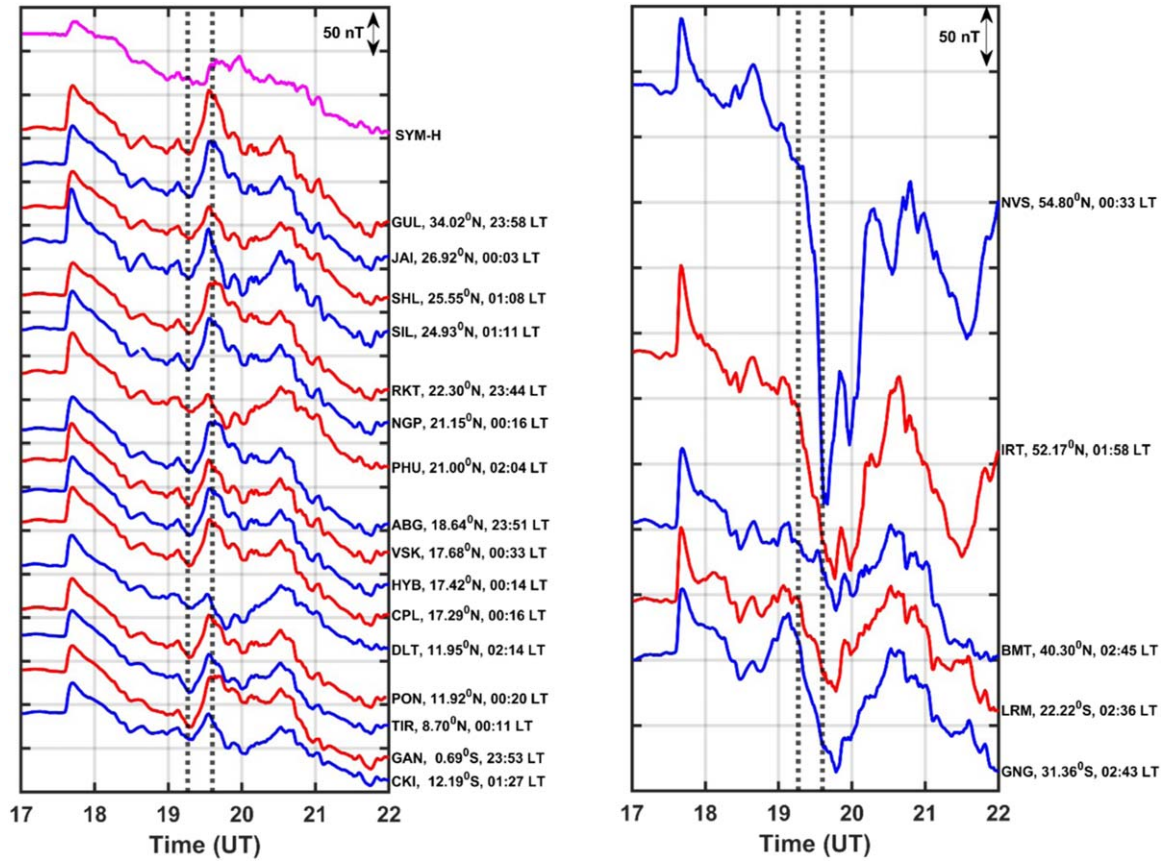

Figure 4. Horizontal magnetic field variation at different latitudes between the 70°E and 115°E longitude sectors. The Sym-H index is shown on top in the left panel. Station code, GGLat, and LT are shown on the right side of each plot. The left and right panels are separated based on the nature of the variation between the two vertical dotted lines.

Table 1
List of Geomagnetic Observatories

S.No.	Station Name	IAGA Code	GGLat	GGLon (°E)	GMLat
1	Gingin	GNG	−31.36	115.72	−40.34
2	Learmonth	LRM	−22.22	114.10	−31.28
3	Cocos-Keeling Islands	CKI	−12.19	96.83	−21.21
4	GAN	GAN	−0.70	73.15	−8.34
5	Tirunelveli	TIR	8.70	77.00	0.63
6	Pondicherry	PON	11.92	79.92	3.6
7	Dalat	DLT	11.95	108.48	2.61
8	Chutuppal	CPL	17.29	78.92	8.99
9	Hyderabad	HYB	17.42	78.55	9.15
10	Visakhapatnam	VSK	17.68	83.32	9.08
11	Alibag	ABG	18.64	72.87	10.82
12	Phuthuy	PHU	21.00	106.00	11.61
13	Nagpur	NGP	21.15	79.10	12.81
14	Rajkot	RKT	22.30	70.93	14.62
15	Sillchar	SIL	24.93	92.82	15.8
16	Shillong	SHI	25.55	91.88	16.45
17	Jaipur	JAI	26.92	75.80	18.78
18	Gulmarg	GUL	34.02	74.42	25.94
19	Beijing	BMT	40.30	116.20	30.95
20	Irkutsk	IRT	52.27	104.50	42.83
21	Novosibirsk	NVS	54.80	83.20	46.03

traversing near dawn is minimal. Interestingly, N19 at ∼7.5 LT showed an electron flux of a few hundred, but N15 at 6.5 LT showed an electron flux of a few tens. The electron flux recorded by N19 was always a few hundred at lower latitudes irrespective of energies and LT and is not consistent with nearby N15 observations. Therefore, we do not interpret N19 electron flux observations here. Near-midnight passes of N18 and M1 showed minimum electron flux at all energies but a few thousand protons of low energies at low latitudes.

5.2. Low-energy Plasma Flux Using Defense Meteorological Satellite Program Observations

Defense Meteorological Satellite Program (DMSP) satellites orbiting at ∼830 km altitude measure low-energy (30 eV–30 keV) electron and proton flux densities, thus providing the broadband plasma flux. K. Shiokawa et al. (1997) have shown the intensification of precipitating BBE flux near the equatorward boundary of the particle precipitation region. Therefore, the BBE signature can be used to identify the equatorward boundary of the auroral activity. Figures 7 and 8 show the DMSP-F18 low-energy plasma flux observations during 19–20 UT in the Northern and Southern Hemispheres, respectively. It is dispensable to mention that the UT intervals in Figures 7 and 8 are different. The magnetic LT was around 5 hr and 3:30 hr in Figures 7 and 8, respectively. At the time of the equatorward boundary crossing of the auroral oval, the DMSP-F18 orbited over 145°E and 110°E GG longitudes during 19–20 UT. We also examined the DMSP-F17 orbits, which were over 160°E and 10°W GG longitudes. Thus, during 19–20 UT on 2023 April 23, DMSP satellites did not exactly orbit over the Indian sector. However, DMSP-F18 passes were in the nearby longitudinal sectors (within 2–4 LT). The

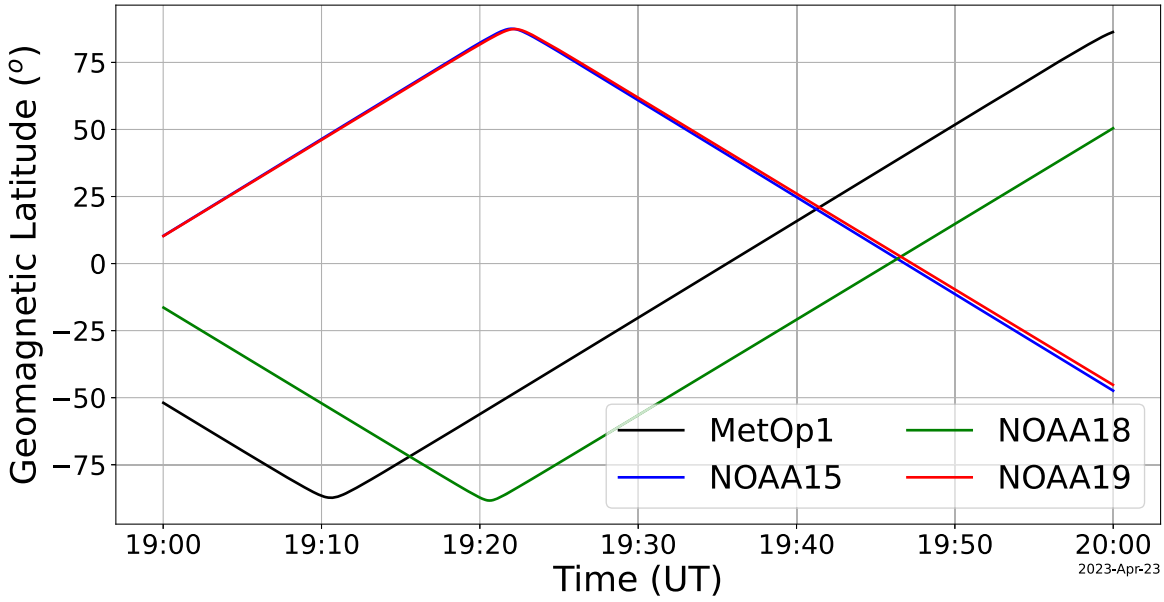

Figure 5. Trajectories (GMLat–time frame) of various NOAA (N15, N18, N19) and Metop1 satellites during 19–20 UT on 2023 April 23.

presence of BBEs is evident in the plots. In Figure 7(b), the equatorward boundary associated with BBEs is found to be at around 54.3° GMLat in the Northern Hemisphere. It can also be observed that the low-energy electrons (<100 eV) are present up to 51.1°N GMLat (54.1° GGLat). These low-energy electrons show a peak flux in ∼50–100 eV at ∼53° GMLat. The low-energy ions are observed up to ∼52°N GMLat. From Figure 8(b), the equatorward boundary is found to be at ∼53°S GMLat in the Southern Hemisphere. The low-energy electrons (a few tens of eV) are observed up to 50°S GMLat.

The global auroral boundaries (both poleward and equatorward) are provided by DMSP, which are based on the auroral particle flux data and fitted GUVI model global boundary. In Figure 9(a), the red dashed curve shows the GG position of the equatorward boundary of the aurora in the Northern Hemisphere at 19:15 UT. It is true that the auroral activity is essentially expressed in geomagnetic coordinates; however, there are a variety of geomagnetic coordinates available, such as centered dipole, corrected geomagnetic, altitude-adjusted corrected geomagnetic, etc., which vary with the altitude and are noncompatible with each other (K. M. Laundal & A. D. Richmond 2017). The LBHS emissions (140–150 nm) captured by the onboard SSUSI sensor are shown on the backdrop indicating the extension of the auroral oval to the lower latitudes. The equatorward boundary in the 4–5 LT sector (that of DMSP-F18) is 59°N GGLat, which is higher than the one obtained from the particle flux data discussed above. Thus, a difference of ∼5° is noticed between global boundary estimates and in situ observations. The boundary in Hanle's longitude (0.5–1.5 LT) is 57°N GGLat. This is more equatorward compared to that in the 4–5 LT sector of DMSP-F18.

5.3. Auroral Oval Boundaries from Swarm

The Swarm mission, consisting of three polar low-Earth-orbiting satellites, provides the parameters related to auroral electrojets named Auroral Electrojet and auroral Boundaries estimated from Swarm observations (AEBS) products. It estimates FACs and derives the auroral oval boundaries based on them by merging electric fields through the Newell coupling function. The details of boundary determination can be found in C. Xiong et al. (2014). They found that the equatorward boundary has a linear dependence on *Dst* and AE indices; however, the equatorward expansion saturates toward high activity. Figure 9(b) shows the auroral oval equatorward boundaries in the Northern Hemisphere derived from small- and medium-scale FACs based on Swarm A satellite observations. The time resolution is 20–25 minutes, representing four values per orbit and considering only those having good quality indicators. It is seen from the plot that during 19–20 UT, the equatorward boundary reached ∼52° GMLat. This is lower than the prestorm values of around 58−60° GMLat and appears to be consistent with the observations from NOAA/POES and the DMSP satellites. The lowering of the equatorward boundary is almost throughout the Indian night (UT +5:30 hr), except near 21 UT.

6. Discussion

The red-colored emission was observed at Hanle, Ladakh, near the northern horizon at a ∼6°–8° elevation angle from the horizon and appeared from ∼19.5 UT until 22 UT on April 23. This time corresponds to postmidnight (1.0–3.5 IST) time on April 24. In fact, a red-colored diffuse aurora was seen on the same night from Xinjiang (44°N GG latitude) in northwest China (CGTN 2023). Also, there were reports of the aurora from Australia and New Zealand (T. McClure 2023). People in Europe and North America also witnessed the northern lights during the same event. However, due to the summertime sunlight in the Northern Hemisphere during April, spectacular auroras could not be noticed near the auroral oval. In the Southern Hemisphere, in Antarctica, the red and green aurora was witnessed (Figure 1 and Supplementary Figure A2).

The aurora on the nightside is usually associated with a substorm phenomenon comprising auroral electrojet currents, leaving a signature in the ground magnetic field measurements. Correspondingly, the auroral indices AL and AE showed the occurrences of substorms during 16–22 UT, and the most intense ones (AL < −1500 nT) occurred during 19–22 UT.

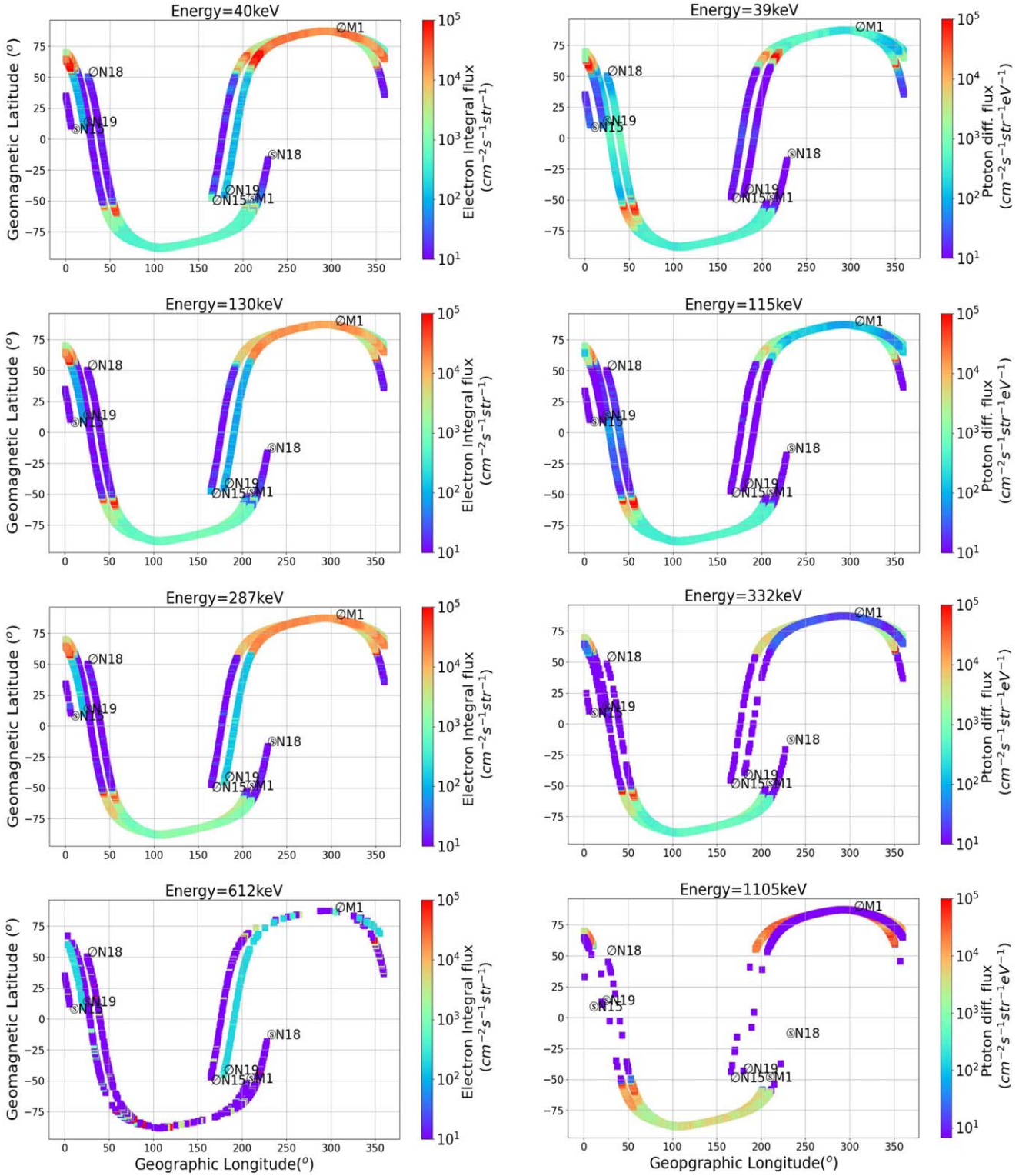

Figure 6. Electron flux (left) and proton flux (right) of various energies in the GMLat–GGLon frame. The color scale is the same in all the plots. The start and end of each satellite trajectory are indicated by Ⓢ and ∅ symbols, respectively.

Nighttime midlatitude Pi2 oscillations, also represented by the Wp index (M. Nosé et al. 2009), are directly related to the sudden development of substorm currents at the onset time leading to the substorm expansion phase. Since the reported event is recent, the Wp index is unavailable. However, we examined the 1 s data from Indian observatories, which were on the nightside. The figure presented in the supplementary material (Figure A1) shows the presence of Pi2 and hence confirms the substorm expansion phase after 19 UT on 2023 April 23, which also coincides with the auroral observations from Hanle.

On 2023 April 23, during the intense substorm activity, the solar wind pressure was quite high, compressing the magnetosphere to 6 R_E (Figure 2). The GOES 16 and 17 satellites were

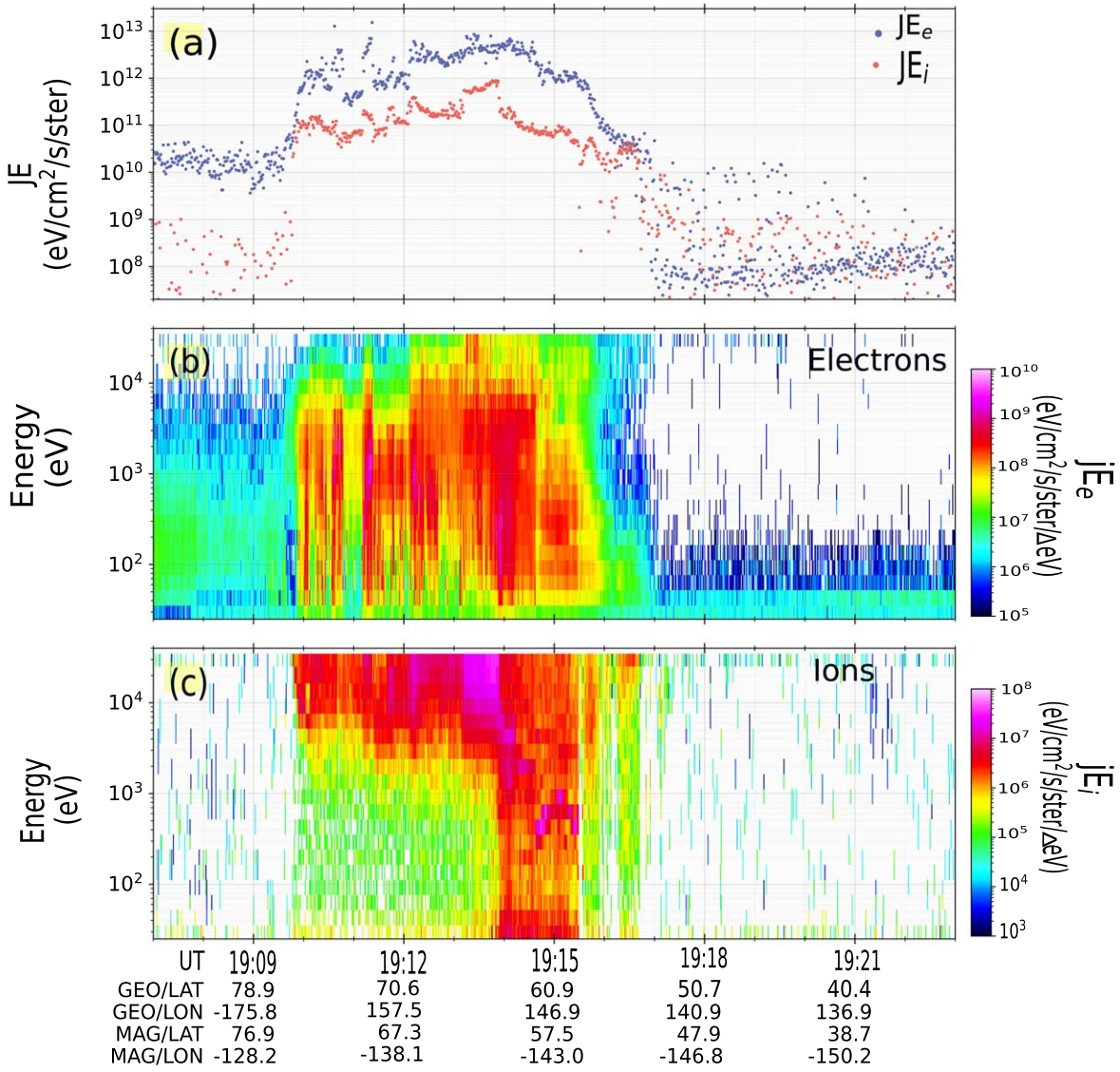

Figure 7. (a) Total particle flux over the Northern Hemisphere in the entire low-energy band for electrons and ions. (b) Energy–time spectra for electrons. (c) Energy–time spectra for ions during 19:07–19:23 UT on 2023 April 23.

outside the magnetosphere (K. Ghag et al. 2024). Such compression during the passage of the ICME sheath along with the prolonged southward IMF might have triggered such an intense substorm on 2023 April 23. Moreover, the solar wind pressure impulse compresses the entire magnetospheric cavity, moving the inner boundary of the tail current sheet closer to the Earth (G. L. Siscoe & W. D. Cummings 1969), which can result in lower-latitude precipitation.

The magnetic signature of the westward auroral electrojet is due to the SCW, which comprises the cross-tail currents, FACs, and ionospheric Hall currents (R. L. McPherron et al. 1973). SCW produces a distinctive magnetic field pattern of the positive bay in the H component at the midlatitude stations located within 21–02 LT hours (C. R. Clauer & R. L. McPherron 1974). We examined the magnetic field variations at the stations from Indian–Asian longitudes (70°−115°E longitude) on the nightside. The storm time magnetic field signatures at mid-to-low latitudes are mainly dominated by the ring current monitored by the Sym-H index, and hence the positive bays in the H variations associated with the SCW system are not easily discernible. The positive H variation between 19.2 and 19.8 UT exhibits bay-type variation, although it was also accompanied by the solar wind dynamic pressure impulse that produced positive variations on the ground. This timing also coincided with the appearance of red-colored aurora at Hanle, an intense AL index, and Pi2 occurrence. The amplitude of positive increase due to the solar wind pressure impulse is ∼25 nT in the Sym-H index, whereas the amplitude of H variation on the nightside midlatitude stations is ∼50 nT, which could be due to the additional contribution of the SCW-related positive bay. Figure 4 indicates that not all midlatitude stations show this positive variation. A rapid and deep depression of 250 nT magnitude in the H component is observed at the NVS (46°N GMLat) station. This depression was seen in both hemispheres at five midlatitude stations located near midnight, reaching up to 31° geomagnetic latitudes. This can indicate the presence of the signature of a substorm at midlatitudes in the Northern and Southern Hemispheres despite the expected positive variation due to the positive bay and solar wind pressure impulse. The high-latitude stations located north of NVS, viz, AMD (62.13°N GMLat), DIK (64.83°N GMLat), and BRN (69.86°N GMLat), show a negative depression in H of magnitude

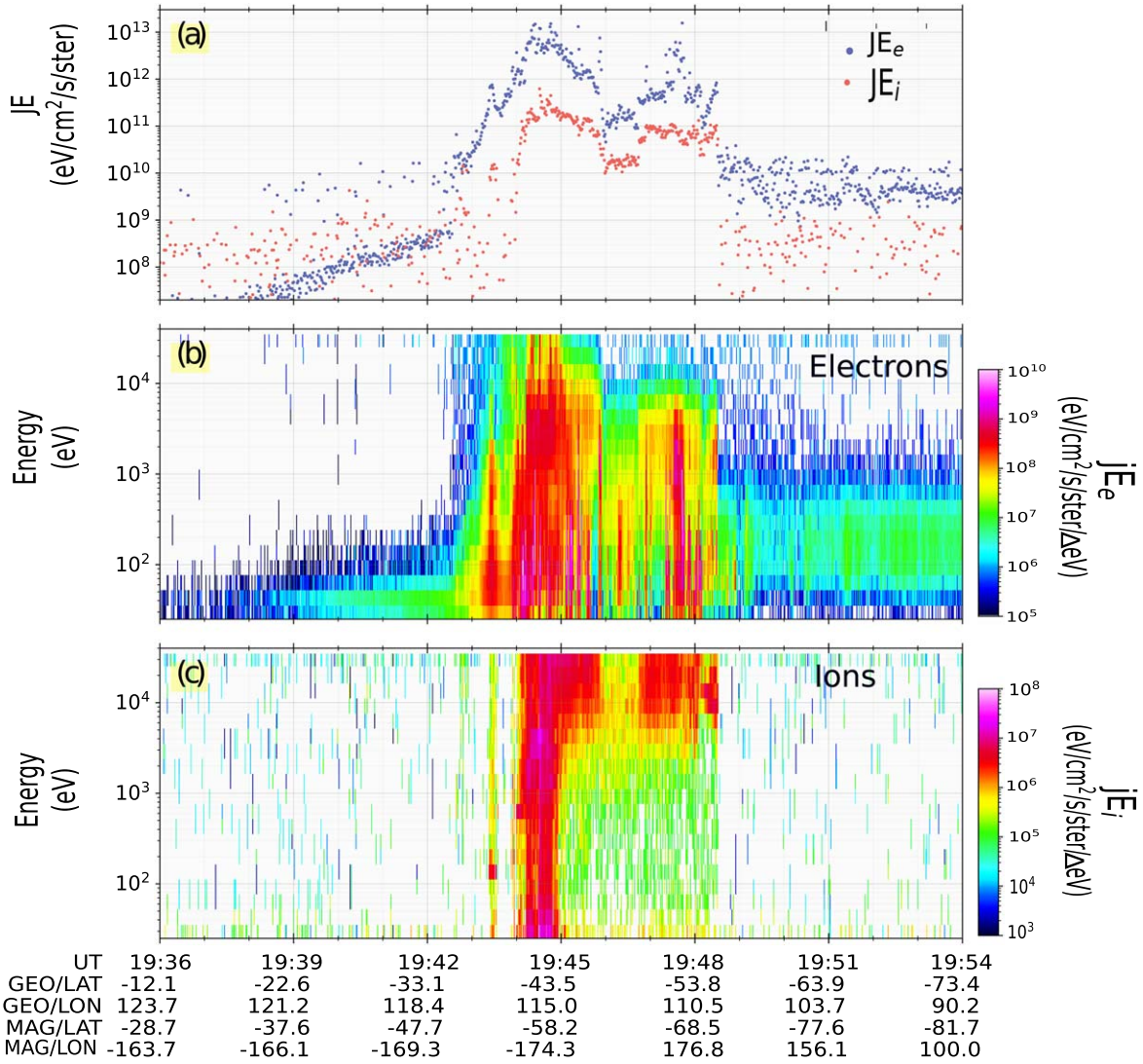

Figure 8. (a) Total particle flux over the Southern Hemisphere in the entire low-energy band for electrons and ions. (b) Energy–time spectra for electrons. (c) Energy–time spectra for ions during 19:38–19:58 UT on 2023 April 23.

1000 nT, 1500 nT, and 500 nT, respectively, indicating a strong westward electrojet/SCW there. Now the question is: does the negative depression at the abovementioned midlatitudes indicate the expansion of the equatorward boundary of the auroral oval? The auroral boundaries observed from the particle flux data in NOAA/POES and the DMSP satellites indicate that the expansion of the equatorward boundary is at least up to ∼52° GMLat at satellite altitudes. This boundary is also consistent with the Swarm-AEBS products of auroral boundaries derived from FACs and the solar wind–magnetosphere coupling function. Thus, it is clear from the particle flux and electric current observations that the boundaries have not shifted below 50°. According to the estimates calculated by S. P. Blake et al. (2021) for a geomagnetic storm with minimum $Dst = -200$ nT, the maximum extent of the auroral equatorward boundary (MEAEB) would be above 50° GMLat. R. G. Landry & P. C. Anderson (2019) found that the equatorward boundary of the diffuse aurora is best described by a weighted average of the AE index, rather than the *Dst* or *Kp* indices. Even with this consideration, the MEAEB is found to be >50°. Thus, the models do not estimate the equatorward boundary to expand below 50° latitude during the substorms with AL ∼−1500 nT, which is also evident from the particle precipitation data of the DMSP satellites and NOAA/POES studied here. Then why are the negative H depression and the aurora observed at low-to-midlatitudes? The signature discussed in the present paper (between two vertical lines in Figure 4) is accompanied by the solar wind pressure impulse, which shows clear positive variation at other lower latitudes and is also expected to have a similar nature at stations like BMT and LRM, unlike the actual observations. The westward auroral electrojet currents flowing in the ionosphere of the auroral oval create negative H variation just below the oval, as well as at lower latitudes than that of the oval. In the absence of overhead quiet-time ionospheric currents at the nightside, the strong auroral ionospheric currents influence the magnetic field signatures at the midlatitudes close to the auroral boundary. Thus, when the H depression has a magnitude of ∼1500 nT in the auroral oval, the lower latitudes still capture the negative H variation of magnitude ∼50 nT. Accordingly, the *Z* variation at these lower latitudes in the Northern Hemisphere is upward (negative), and it is downward (positive) in the Southern Hemisphere.

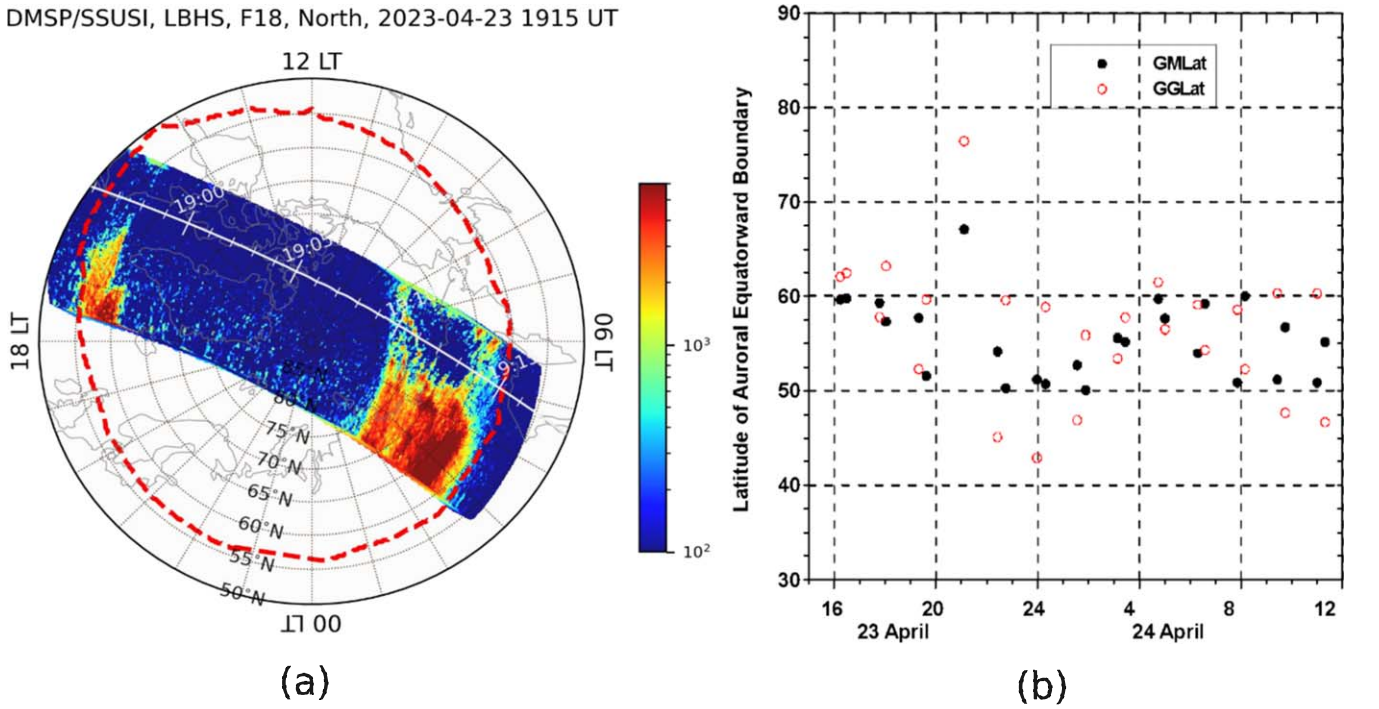

Figure 9. Equatorward auroral boundary based on (a) DMSP-F18 observations and the fitted GUVI model global boundary (GGLat red dashed curve) and (b) Swarm (GGLat, red open circles, and GMLat, black filled circles) for the Northern Hemisphere during 2023 April 23–24.

Many researchers have attributed the source of the diffused red aurora to the hot electrons coming from the central plasma sheet (R. B. Horne & R. M. Thorne 2000; R. M. Thorne et al. 2010; J. Liang et al. 2011; B. Ni et al. 2011; J.-C. Zhang et al. 2014; Y. Nishimura et al. 2022). The DMSP observations of low-energy plasma (10 eV–30 keV) indicate the precipitation of BBE flux at the equatorward boundary of the auroral precipitation, which originates from the inner part of the plasma sheet and is attributed as a possible cause of the red aurora observed at midlatitudes (K. Shiokawa et al. 1997). The low-energy electrons of BBEs interact with the oxygen atoms at higher altitudes of ~600 km and cause red color emissions (630.0 nm; K. Shiokawa et al. 1996, 1997), whereas higher-energy electrons penetrate deeper into the ionosphere, causing a green color aurora (577.7 nm) on interaction with oxygen at a ~100–300 km height. The observed aurora at Hanle was not overhead; rather, it was seen near the northern horizon. The observed red color appeared diffused, without a sharp boundary. Using the background star positions in the sky and the simulated night sky by the Stellarium planetarium software, the elevation angle (β) of the observed red light is estimated as 6°–8°. Figure 10 shows the schematic geometry of the auroral visibility at the observer. The auroral emissions occur over point "A" at a height of "h" from the surface of the Earth. Angle θ_A is the latitude of A, and θ_o is the latitude of the observer location "O." If the angle of elevation (β) of auroral light at point "O" is known, then the height of auroral emissions over point "A" can be calculated as

$$h = \frac{a.\cos(\beta)}{\cos(\beta + (\theta_A - \theta_o))} - a, \quad (1)$$

where "a" is the radius of Earth, 6370 km. Point "B" is the location where auroral emissions will be at the horizon, i.e., $\beta = 0$, so it can be considered as the lowest latitudinal boundary of the auroral visibility. For the red aurora occurring over point A at 600 km altitude, the aurora will be seen within a periphery of the radius of angle ~22°. The scattering effects due to a dense atmosphere are found to be less than half a degree. From the previous sections, we find that during the studied time interval of the 2023 April 23 storm, the low-energy electrons precipitate up to $\theta_A = 54°$N GGLat in the 4–5 LT sector. Unfortunately, we do not have these observations from the near-midnight sector, where Hanle was located. Therefore, we estimate θ_A in this LT sector by using the Hanle observations of $\beta = 6°$–8° at $\theta_o = 33°$ GGLat with some standard emission altitude. F. Roach & E. Marovich (1960) estimated the visible auroral altitude as 400 km, whereas K. Shiokawa et al. (1996) estimated the height of the red aurora as ~600–650 km. Using Equation (1), with 400 km altitude, θ_A is estimated to be 47°N GGLat, while, with the emission altitude of 600–650 km, we find θ_A to be around 52°N GGLat, which is closer to the particle precipitation observations shown in the other nearby LT sectors. This means that in the near-midnight sector, the equatorward boundary of the auroral oval has moved further toward the equator by 2° compared to that in the 4–5 LT sector, when an emission altitude of 600–650 km is considered. The global auroral boundaries depicted in Figure 9(a), which are derived from the DMSP data and a fitted GUVI model, indicate the equatorward boundary in the midnight sector at around 57°N. The model-estimated boundary in the 4–5 LT sector is 59°N, which is higher by ~5° than the actual observations (54°N GGLat). Therefore, the equatorward boundary in the midnight sector can be considered as 52°N GGLat, which matches with the estimates calculated above, using Hanle observations and Equation (1). Thus, the red color emissions occurring at 52°N GGLat at the height

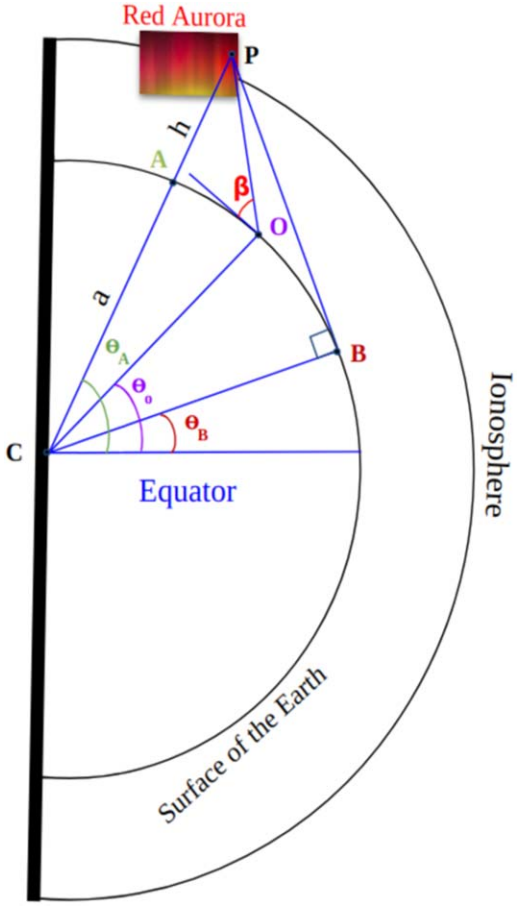

Figure 10. Sketch showing the geometry of auroral visibility at observer latitude (θ_o). *C* is the center of the Earth; *a* is the radius of the Earth, 6370 km; *P* is the point of auroral precipitation at height "*h*" km at GGLat θ_A, and *A* is the point on the surface of the Earth. *B* is the tangent point at the surface of the Earth line originating from point *P*, and θ_A is the latitude of that point. β is the maximum elevation angle of the aurora seen by the observer. The sketch is not to scale.

~600–650 km would be responsible for the observed aurora at Hanle. The green aurora produced at ~100 km can be seen within the periphery of 10° and cannot be visible from low latitudes. Though the combination of green, red, and blue auroras was present in the auroral oval (Figure A2 from Antarctica), the red color is prominently seen from the lower latitudes, due to its higher altitudes. This is why the low-to-midlatitude aurora is normally red (B. A. Tinsley et al. 1986).

Also interestingly, the NOAA/POES observations show that although the integral flux of low-energy (40 keV) protons is maximum in the auroral oval, a few thousand (two orders smaller than the maximum) protons precipitated at lower latitudes in the midnight sector, whereas the precipitating electron flux is minimum therein. The waves generated by the solar wind pressure impulse, such as Pi2 and EMIC, could be responsible for the scattering of plasma particles from the ring current, which follow the magnetic field lines. However, the presence of particles close to the equator is intriguing.

7. Conclusions

On the night of 2023 April 23–24, Hanle observatory in Ladakh, India, observed a red-colored light glow in the north direction with the all-sky camera having a 180° field of view that was claimed as an aurora. This is the first observational imaging evidence of a low-latitude aurora in India, unlike the past historical records of the phenomenon through human naked-eye observations. It is extremely rare to observe auroras at such low latitudes during a moderate geomagnetic storm. However, the contemporary observation of low-latitude auroras, combined with in situ multispacecraft particle measurements and both ground-based and satellite-based magnetic field data, offers significant insights into the phenomenon. Following are the concluding remarks.

1. Intense substorms occurred during the period of red aurora observations from Ladakh.
2. In situ plasma particle data and Swarm mission AEBS products show that the equatorward boundary of the auroral precipitation has moved toward lower latitudes compared to other active periods (up to 52° geomagnetic latitude), although it has not reached Indian latitudes.
3. Occurrence of BBE events with electron energies <100 eV at 54°N GGLat in the 4–5 LT sector is found. The equatorward boundary in the midnight sector is estimated as 52°N GGLat, using Hanle observations in the simple calculations with the low-energy electron emission altitudes as 600–650 km.
4. Thus, the red aurora observed from the lower latitudes is unequivocally the result of two factors: a slight expansion of the equatorward boundary of the auroral oval and high-altitude red emissions due to enhanced low-energy electron precipitation in the auroral oval. It is important to note that the low-latitude aurora is not because of the equatorward boundary of the auroral oval reaching that latitude.
5. Negative H variation at nighttime midlatitudes below the equatorward boundary of auroral precipitation is observed, which could be due to the contribution of the magnetic field associated with the westward auroral electrojet currents flowing in the ionosphere of the auroral oval.

Acknowledgments

The authors acknowledge the IIA's all-sky camera observation records at Hanle, India, and NCPOR's All-Sky Camera observations from Maitri station, Antarctica. The NCPOR contribution number is J-41/2024-24. We acknowledge the INTERMAGNET and IIG magnetic observatory network for providing ground geomagnetic field data. We thank WDC Kyoto for providing geomagnetic indices and the Space Physics Data Facility/Goddard Space Flight Center OMNIWeb Interface (https://omniweb.gsfc.nasa.gov/) for providing solar wind and IMF data. The authors acknowledge the DMSP, NOAA/POES, and the Swarm mission for the data used in the present study. The solar wind parameters, interplanetary magnetic field, and geomagnetic indices used in this study are obtained from CDAWEB (https://cdaweb.gsfc.nasa.gov/) and SuperMAG (http://supermag.jhuapl.edu/).

Appendix
Supplementary Information

Geomagnetic substorm onsets are complemented by the occurrence of Pi2 pulsations at low latitudes on nightside. Figure A1 uses the horizontal component of magnetic field with one second time resolution at five Indian magnetic

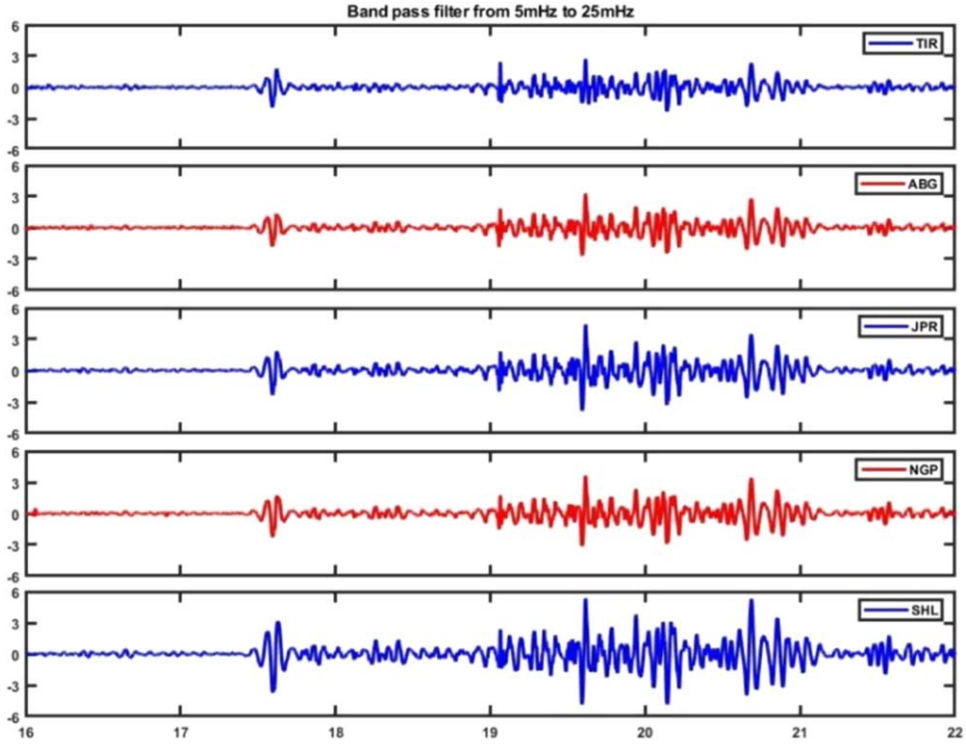

Figure A1. Pi2 pulsations observed at low-latitude night stations; bandpass between 5 and 25 mHz.

(a) (b)

Figure A2. Aurora seen from Indian Antarctic station Maitri on 2023 April 23: (a) photograph at 22:01 UT, (b) all-sky camera at 19:22 UT.

observatories viz. Tirunelveli (TIR), Alibag (ABG), Jaipur (JPR), Nagpur (NGP), and Shilong (SHL). The plots in the Figure A1 are obtained by band passing the H-variations between 5 and 25 mHz and show the presence of Pi2 oscillations between 19 and 21 UT. Figure A2 displays the aurora observations from Indian Antarctic station, Maitri.

ORCID iDs

Geeta Vichare https://orcid.org/0000-0003-3607-6923
Ankush Bhaskar https://orcid.org/0000-0003-4281-1744
Virendra Yadav https://orcid.org/0000-0002-9058-1835

References

ABP Live 2023, WATCH: Never-Before-Seen auroras illuminate Ladakh skies in rare event as geomagnetic storm hits Earth, ed. radifahk https://news.abplive.com/science/auroras-india-watch-never-before-seen-auroras-illuminate-ladakh-skies-in-rare-event-as-geomagnetic-storm-hits-earth-indian-institute-of-astrophysics-indian-astronomical-observatory-hanle-1599274
Akasofu, S.-I. 1964, P&SS, 12, 273
Anand, A. 2023, Old, Unrelated Pictures Shared as 'Aurora Borealis in Ladakh', The Quint, https://www.thequint.com/news/webqoof/aurora-borealis-northern-lights-ladakh-fact-check/#read-more
Baker, D. N., Pulkkinen, T. I., Angelopoulos, V., Baumjohann, W., & McPherron, R. L. 1996, JGR, 101, 12975
Behera, J. K., Sinha, A. K., Singh, A. K., et al. 2015, AdSpR, 56, 28

Bhaskar, A., Hayakawa, H., Oliveira, D. M., et al. 2020, JGRA, 125, e2020JA028227
Bhaskar, A., & Vichare, G. 2013, JGRA, 118, 4696
Blake, S. P., Pulkkinen, A., Schuck, P. W., Glocer, A., & Tóth, G. 2021, JGRA, 126, e2020JA028284
CGTN 2023, Stunning auroras amaze skywatchers in Xinjiang, NW China, CGTN, https://news.cgtn.com/news/2023-04-25/Stunning-auroras-amaze-skywatchers-in-Xinjiang-NW-China–1jhO0ZViIAU/index.html
Clauer, C. R., & McPherron, R. L. 1974, JGR, 79, 2811
Cole, K. D. 1965, JGR, 70, 1689
Dai, L., Han, Y., Wang, C., et al. 2023, ApJ, 945, 47
Davis, T. N., & Sugiura, M. 1966, JGR, 71, 785
DeJong, A. D., Cai, X., Clauer, R. C., & Spann, J. F. 2007, AnGeo, 25, 1865
ET Online and Agencies 2023, Rare Northern lights witnessed in Ladakh; not an "air glow", confirms Hanle sources, The Economic Times, https://economictimes.indiatimes.com/news/india/aurora-rare-northern-lights-witnessed-in-ladakh/articleshow/100048221.cms?from=mdr
Gallardo-Lacourt, B., Frey, H. U., & Martinis, C. 2021, SSRv, 217, 1
Ghag, K., Raghav, A., Bhaskar, A., et al. 2024, AdSpR, 73, 6288
Gonzalez, W. D., Joselyn, J. A., Kamide, Y., et al. 1994, JGR, 99, 5771
Hajra, R., & Tsurutani, B. T. 2018, ApJ, 858, 123
Hayakawa, H., Cliver, E. W., Clette, F., et al. 2023, ApJ, 959, 23
Hayakawa, H., Ebihara, Y., Hand, D. P., et al. 2018a, ApJ, 869, 57
Hayakawa, H., Nevanlinna, H., Blake, S. P., et al. 2022, ApJ, 928, 32
Hayakawa, H., Vaquero, J. M., & Ebihara, Y. 2018b, AnGeo, 36, 1153
Horne, R. B., & Thorne, R. M. 2000, JGRA, 105, 5391
IIABengaluru 2023, X, https://x.com/IIABengaluru/status/165225978208-5210113
Kilpua, E. K. J., Olspert, N., Grigorievskiy, A., et al. 2015, ApJ, 806, 272
Kim, H., Shiokawa, K., Park, J., et al. 2021, GeoRL, 48, e2021GL095090
Kozyra, J. U., & Liemohn, M. W. 2003, Ring Current Energy Input and Decay (Berlin: Springer), 105
Kozyra, J. U., Nagy, A. F., & Slater, D. W. 1997, RvGeo, 35, 155
Landry, R. G., & Anderson, P. C. 2019, JGRA, 124, 2072
Laundal, K. M., & Richmond, A. D. 2017, SSRv, 206, 27
Lee, P.-H., & Liu, J.-Y. 2023, EP&S, 75, 138
Liang, J., Ni, B., Spanswick, E., et al. 2011, JGRA, 116, A12220
MacDonald, E. A., Donovan, E., Nishimura, Y., et al. 2018, SciA, 4, eaaq0030
McClure, T. 2023, Aurora Australis lights up New Zealand skies in spectacular "solar tsunami", The Guardian, https://www.theguardian.com/world/2023/apr/25/aurora-australis-new-zealand-sky-spectacular-light-show-solar-tsunami-southern-lights
McPherron, R. L. 1972, P&SS, 20, 1521
McPherron, R. L., Russell, C. T., & Aubry, M. P. 1973, JGR, 78, 3131
Newell, P., & Gjerloev, J. 2011, JGRA, 116, A03229
Ni, B., Thorne, R. M., Meredith, N. P., Horne, R. B., & Shprits, Y. Y. 2011, JGRA, 116, A03208
Nishimura, Y., Bruus, E., Karvinen, E., et al. 2022, JGRA, 127, e2022JA030570
Nomura, R., Shiokawa, K., Omura, Y., et al. 2016, JGRA, 121, 1608
Nosé, M., Iyemori, T., Takeda, M., et al. 2009, in Proc. of 13th IAGA Workshop on Geomagnetic Observatory Instruments, Data Acquisition, and Processing, US Geol. Surv. Open File Rep, 1226, Citeseer (Reston, VA: USGS), 202
Oliveira, D. M., Hayakawa, H., Bhaskar, A., Zesta, E., & Vichare, G. 2020, EP&S, 72, 1
Raghav, A. N., Kule, A., Bhaskar, A., et al. 2018, ApJ, 860, 26
Rao, M. P. 1964, MAUSA, 15, 639
Roach, F., & Marovich, E. 1960, JRNBS, 64, 205
Rostoker, G., Akasofu, S.-., Foster, J., et al. 1980, JGR, 85, 1663
Sakaguchi, K., Shiokawa, K., Miyoshi, Y., & Connors, M. 2015, Auroral Dynamics and Space Weather, Vol. 215 (New York: Wiley), 59
Shiokawa, K., Meng, C.-., Reeves, G. D., Rich, F. J., & Yumoto, K. 1997, JGR, 102, 14237
Shiokawa, K., Yumoto, K., Meng, C.-I., & Reeves, G. 1996, GeoRL, 23, 2529
Silverman, S. M. 2003, JGR, 108, 8011
Silverman, S. M. 2008, JASTP, 70, 1301
Siscoe, G. L., & Cummings, W. D. 1969, P&SS, 17, 1795
Thorne, R. M., Ni, B., Tao, X., Horne, R. B., & Meredith, N. P. 2010, Natur, 467, 943
Tinsley, B. A., Rohrbaugh, R., Rassoul, H., et al. 1986, JGR, 91, 11257
Uberoi, C. 2011, SpWea, 9, S08005
Vaquero, J. M., Gallego, M. C., & Domínguez-Castro, F. 2013, GeofI, 52, 87
Vaquero, J. M., Trigo, R. M., & Gallego, M. C. 2007, EP&S, 59, e49
Vemareddy, P. 2024, ApJ, 961, 199
Vichare, G., Alex, S., & Lakhina, G. 2005, JGRA, 110, A03204
Wang, G., Yao, S., Yu, Y., et al. 2021, ApJ, 908, 187
Willis, D., Stephenson, F. R., & Fang, H. 2007, AnGeo, 25, 417
Xiong, C., Lühr, H., Wang, H., & Johnsen, M. G. 2014, AnGeo, 32, 609
Zhang, J.- C., Saikin, A. A., Kistler, L. M., et al. 2014, GeoRL, 41, 4101